Experiments in Fluids 33 (2002) 545–554
DOI 10.1007/s00348-002-0486-8

Photobleached-fluorescence imaging of microflows

B.P. Mosier, J.I. Molho, J.G. Santiago

Abstract A photobleached-fluorescence imaging technique for visualizing microscale flow fields and obtaining molecular diffusion and advection information has been developed. The technique tracks fluorophores in the region of a photobleached line in a planar microdevice and yields quantitative diffusive and advective transport data. Visualizations of two- and weakly three-dimensional electroosmotically and pressure-driven fluid flow fields are demonstrated using the photobleaching of fluorescein and fluorescein-dextran conjugates. Photobleached-fluorescence imaging tracks undisturbed fluorophores, functions in polymer and glass microfluidic devices, can take advantage of fluorescent conjugates present in biochemical assays, and has a photobleached region that is flow independent.

List of symbols

a_z	capillary depth
a_y	capillary width
b_x	beam width in x at the beam waist
b_y	beam width in y at the beam waist
c	fluorophore concentration
d_z	collimated beam dimension
e	electron charge
E	electric field
f	focal length
I	pixel intensity
I_{corr}	corrected image
I_{df}	darkfield image
I_{ff}	flatfield image (uniform illumination on a uniformly seeded field)
I_L	laser intensity of beam exiting the microscope objective
I_{raw}	raw image
ID	inner diameter
k	thermal conductivity of water
M	molarity (moles/liter)
N_A	Avogadro's number
NA	numerical aperture
OD	outer diameter
$\dot{q}'''$	rate of heat generation per unit volume
QE	quantum efficiency
R	universal gas constant
T	temperature
t_b	duration of photobleaching pulse
u	electroosmotic velocity
U_{APP}	apparent velocity of photobleached zone
U_{EOF}	electroosmotic velocity of tracer
U_{EP}	electrophoretic velocity of tracer
z	valence number

Greek symbols

α	thermal diffusivity of water
ϵ	permittivity of water
λ	argon ion laser wavelength
μ	dynamic viscosity of water
ν	ionic mobility
ω	molar absorptivity
σ_L	laser half-width
χ	area fraction of laser sheet incident on fluid
ζ	zeta potential

Received: 7 February 2001 / Accepted: 29 April 2002
Published online: 14 August 2002

B.P. Mosier (✉)
Sandia National Laboratories,
7011 East Ave. MS9951, Livermore, CA 94550, USA
E-mail: bpmosie@sandia.gov
Tel.: +1-925-2943569
Fax: +1-925-2943020

J.I. Molho
Caliper Technologies Corp.,
605 Fairchild Dr., Mountain View, CA 94043, USA

J.G. Santiago
Mechanical Engineering Department, Thermosciences Div.,
Stanford University, Bldg. 500 Rm. 500Y, Stanford, CA 94305, USA

This work was sponsored by DARPA Grants Nos. F30602–00–2-0609 and F33615–98–1–2853 with Drs. Anantha Krishnan and Abraham Lee as contract monitors, respectively. J.I.M. is supported by a Hewlett-Packard Stanford Graduate Fellowship. The authors would like to thank Dr. James Mikkelsen, Jr. for helpful discussions and advice.

1 Introduction

The development of complex microfluidic systems (Dolnik et al. 2000, Effenhauser 1998, Manz et al. 1993) requires detailed visualizations of species concentrations in microscale flow fields. Detailed flow visualizations help characterize system performance, identify non-ideal flow characteristics, and validate simulation efforts. Photobleaching has been used in the last few decades to study diffusion across cell membranes and within cells (Axelrod et al. 1976) in a technique called fluorescence recovery after photobleaching (FRAP). There are several FRAP techniques and analysis methods including modulation FRAP (Lanni and Ware 1982), video FRAP (Salmon et al.

1984), and spatial Fourier analysis FRAP (Tsay and Jacobson 1991). Photobleaching has also been used in an on-column sample gating technique for capillary zone electrophoresis (CZE) and high-performance liquid chromatography (Monnig and Jorgenson 1991, Monnig et al. 1991). Moore and Jorgenson (1993) used on-column sample gating to examine analyte dispersion in CZE. More recently, photobleaching has been used to monitor volume-averaged bulk electroosmotic flow (EOF) in a point-wise detection scheme applied to a capillary electrophoresis system (Schrum et al. 2000). Other non-elastic scattering techniques that image optical patterns onto dye solutions in order to visualize the flow include: molecular tagging velocimetry (MTV) of phosphorescent supramolecules (Koochesfahani et al. 1996), caged-fluorescence imaging (Lempert et al. 1995, Paul et al. 1998), laser-induced photochemical anemometry (Falco and Chu 1987), and laser-induced fluorescence (Wang and Fiedler 2000a, 2000b).

We have developed a flow imaging technique that uses the photobleaching of dilute solutions of fluorescein and fluorescein-dextran conjugates to visualize flow timelines and concentration fields in microchannels with characteristic dimensions of order 100 μm. We present here the design of a photobleached-fluorescence imaging system including a description of optical components, timing, and the resulting measurement volume characteristics. Application of the technique to electrokinetic systems requires quantifying dye transport properties such as electrophoretic mobility and molecular diffusivity. This is achieved by visualizing the transport of the dye in a system that simultaneously applies the current monitoring method (Huang et al. 1988). Microscale flow visualizations of electrokinetically and pressure-driven flow in glass capillaries and acrylic microchannels are presented. The relevant constraints on chemistry, geometry, materials, and heat transfer necessary for the proper application of the technique are described.

1.1 Photobleaching

A study of the photobleaching kinetics of fluorescein in aqueous solution by Song et al. (1995) demonstrates photobleaching as a process in which a high-intensity light source chemically changes a fluorophore so that it no longer participates in the absorption/emission process. The rate of fluorescein photobleaching depends on the photon flux. In the current work, photobleaching takes place on the order of milliseconds. Typical bleach pulse lengths are 10–100 ms, while typical camera exposure times are 10–50 ms. For a fluid volume of 25,000 μm^3, a fluorescein concentration of 1 mM, and a laser beam power of 12 mW, the fluorescence intensity decreases by 30% within 10 ms. These time scales allow flow tagging to be performed in most microfluidic flows of interest. A dilute solution of a highly fluorescent molecule such as fluorescein is used as a flow tracker. A brief exposure to a laser sheet photobleaches some fraction of the fluorophores in the flow, resulting in a photobleached molecular species concentration distribution of the form $(I_o - I)$, where I is the laser sheet intensity profile and I_o is a normalization constant. The intensity distribution associated with the fluorescence of undisturbed/unphotobleached molecules is then imaged using a microscope objective and a CCD array. The development of the photobleached region (both diffusion and advection effects) is then used to determine flow field conditions and transport coefficients such as electrophoretic mobility and diffusivity. Photobleached-fluorescence imaging has several advantages over other microflow visualization techniques. First, although photobleaching may change the mobility of dye molecules, the visualization deals strictly with undisturbed/unphotobleached fluorophores. Since the fluorophore concentration is dilute (typically less than 1 mM), the visualized molecule's electromigration and diffusion are independent of the photobleached/disturbed molecules. A second advantage is that both polymer and glass microfluidic systems are transparent to visible laser light (e.g., 488-nm argon ion line). This characteristic is in contrast to caged-fluorescence imaging techniques that typically require ultraviolet light to activate the caged dye molecules (Herr et al. 2000; Paul et al. 1998). A third advantage is that the technique can be used with fluorophores already present in many bioanalytical assays (e.g., fluorescein-isothiocyanate-protein conjugates). One disadvantage of the technique compared to caged-fluorescence imaging techniques is that the signal-to-noise ratio (SNR) that defines image contrast (see image correction section below) is currently as much as one order of magnitude lower for photobleached-fluorescence imaging. One reason for the different SNRs is that, for the negligible-temperature-rise application investigated here, not all molecules in the photobleaching area are photobleached.

There are several parameters to consider when using photobleached-fluorescence imaging. First, the duration of useful image SNR is limited by molecular diffusion and shear-driven dispersion of the photobleached zone. In the current experiments, we use both fluorescein and fluorescein-dextran conjugate with mass diffusivities of 5×10^{-6} and 9×10^{-8} $cm^2\times s^{-1}$, respectively. An interesting figure of merit is the characteristic time for fluorophore diffusion across the half-width of the laser sheet. For our fluorescein and fluorescein-dextran conjugate tracers, these times are 50 ms and 4 s, respectively. This time can be used to select a Peclet number (Probstein 1994) appropriate for the visualization and/or application. Out-of-image-plane velocity gradients will disperse the scalar and result in a smaller useful time scale. Another physical constraint arises from the system optics; the depth of the microflow device must be less than the collimated range for the laser to achieve a uniform photobleaching zone throughout the depth of the probe volume. Also, the highest flow velocity that can be analyzed is a function of the fluorophore photobleaching time and the desired image magnification. Finally, the fluorophore concentration must be dilute enough to avoid the inner filter and reabsorption effects and disturbance of the flow through heat absorption. A sufficiently dilute concentration also results in a fluorescence intensity that is proportional to the fluorophore concentration (Tanke et al. 1982).

Reversible photobleaching can occur depending on solute, solvent, and analyte interactions, and is a rapid

process (order of μs). However, in aqueous solutions of borate buffer, water, and fluorescein or fluorescein-dextran conjugates, reversible photobleaching is negligible (Axelrod et al. 1976; Periasamy et al. 1996; Saylor 1995). This observation has been confirmed in the current study by photobleaching an entire microchannel cell and monitoring the fluorescence over periods of several hours. In all cases, photobleached fluorescein solutions remained photobleached.

1.2 Temperature and pH effects

Most bioassays have temperature-sensitive analytes. We have developed a heat transfer model to estimate the temperature rise caused by the photobleaching process. Previous studies of thermal heating in FRAP experiments have examined a finite disk heat source in an infinite fluid (Axelrod 1977) and a cylindrical absorber in an infinite medium (Simon et al. 1988). In the current work, absorption of the photobleaching laser sheet is assumed to be uniform in the direction of beam propagation and along the length of the light sheet; thus the problem may be modeled as one-dimensional heating due to a Gaussian heat source (consistent with the intensity profile of the laser). To be conservative in our maximum temperature estimate, we have chosen to neglect heat conduction through the water perpendicular to the axial direction and the conduction of heat through the channel substrate (a more accurate assumption in the case of the acrylic channels). Assuming that the fluid is an infinite medium with constant properties, that the fluid is initially at a uniform temperature, and that all of the heating comes from absorption of the laser light by fluorescein, the heat equation may be written as

$$\alpha\nabla^2 T + \frac{\alpha}{k}\dot{q}''' = \frac{\partial T}{\partial t}, \tag{1}$$

where the first term on the left-hand side is the diffusion of heat within the fluid, the second term is the heat generation associated with the laser pulse, and the right-hand side is the rate of energy accumulation. The laser heat generation term may be written as

$$\dot{q}''' = \frac{I_L \omega c \chi (1 - QE)}{a\sigma_L\sqrt{2\pi}} \exp\left(-\frac{x^2}{\sigma_L^2}\right). \tag{2}$$

This relation for the rate of heat generation per unit volume, $\dot{q}'''$, is similar to that formulated by Axelrod (1977). The laser energy is in terms of the incident laser beam power, I_L, the channel width, a, and the laser sheet width, σ_L. The fraction of laser energy converted to heat is a combination of the absorption per unit length (molar absorptivity), ω, the concentration, c, and the fraction of light absorbed that does not result in fluorescence, 1-QE. The exponential term describes the variation of the Gaussian laser beam along x, the axial dimension along the channel. The collimated range in the y direction of our setup is substantially larger than the microchannel width, so that a significant fraction (78%) of the laser energy transmitted through the objective falls outside the fluid. Substituting Eq. 2 into Eq. 1 and normalizing the various terms using:

$$x' \equiv \frac{x}{\sigma_L},\ t' \equiv \frac{t}{t_b},\ \theta \equiv \frac{T - T_o}{T_o} \tag{3}$$

$$\frac{\partial\theta}{\partial t'} = c_1 \frac{\partial^2\theta}{\partial x'^2} + c_1 c_2 \exp\left(-x'^2\right), \tag{4}$$

where c_1 and c_2 are dimensionless constants defined as

$$c_1 = \frac{\alpha t_b}{\sigma_L^2},\ c_2 = \frac{\sigma_L I_L \omega c \chi (1 - QE)}{T_o k a \sqrt{2\pi}}. \tag{5}$$

The assumption that the heating results only from absorption by solute fluorescein ions is valid for the concentrations considered here as discussed by Axelrod (1977). Assuming a very long channel and the initial condition θ=0, the temperature rise, ΔT, may be obtained using an infinite-space, time-dependent Green's function:

$$\Delta T(0,t) = \frac{\sigma_L I_L \omega c \chi (1 - QE)}{k a \sqrt{8\pi}} \left[\left\{1 + \frac{4\alpha t}{\sigma_L^2}\right\}^{1/2} - 1\right]. \tag{6}$$

For typical experimental conditions, σ_L=5×10^{-6} m, ω=7.69×10^6 M^{-1}×m^{-1}, QE=0.93, χ=0.12, α=1.45×10^{-7} m^2×s^{-1}, k=0.61 W×m^{-1}×K^{-1}, and a=5×10^{-5} m. Using these values, the temperature rise after a 10-ms pulse of a 100-mW laser pulse is between 2 and 3°C for fluorescein concentrations of c=500 μM to 1 mM. Again, this is a rather conservative estimate because the channel substrate often has a higher thermal diffusivity than water and helps cool the region of interest. In our experiments, we observed no boiling of the fluid and no outgassing of dissolved gas due to a decreased solubility (which is temperature-dependent) even for laser-light exposure times greater than 1 s. Given these observations and the simple analysis above, we concluded that the short time pulses used in our experiment (<10 ms) did not cause heating of the fluid above a few degrees Celsius.

An important parameter in any fluorescence visualization experiment is the pH of the solution. As discussed in detail by Sjoback et al. (1995), the quantum yield, charge state, and absorption/emission spectra of fluorescent dyes are strong functions of pH. An important consideration therefore is the effects of electrolysis on pH uniformity for a given volume of the buffer wells, electric field, capillary cross-sectional area, fluid composition, and zeta potential (Bello 1996). To minimize total system current and associated pH changes in the capillary, we have used relatively small cross-sectional area channels ranging from 50×50 μm to 50×500 μm with relatively large reservoirs (volumes greater than 10 μl). We have employed 20 mM borate buffer and electric fields ranging from 30 to 80 V×cm^{-1}. Testing of the reservoir fluid pH at the beginning and end of typical experiments revealed no significant pH change.

2 Experimental setup

A schematic of the experimental setup is shown in Fig. 1a. The main component is an epifluorescent microscope

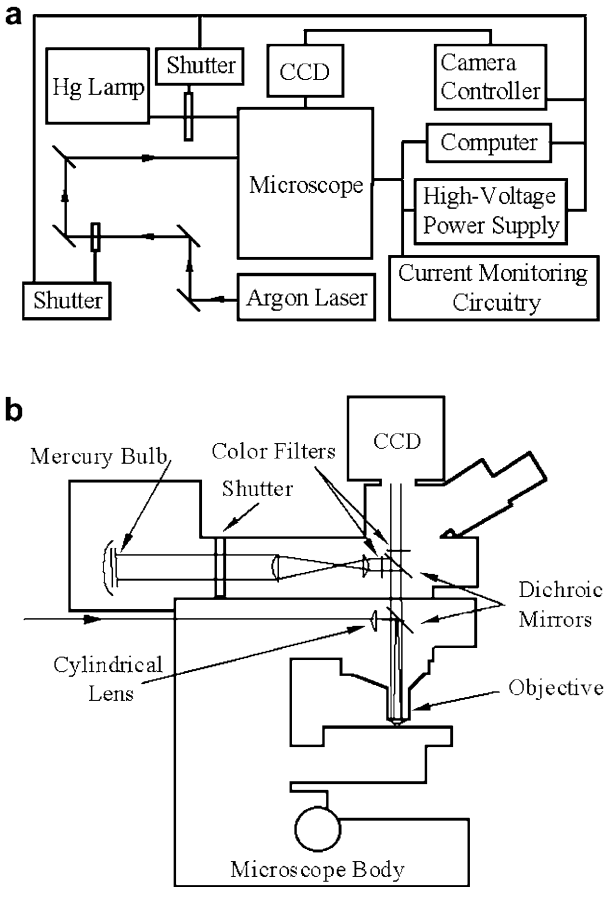

Fig. 1. **a** Schematic of the photobleached-fluorescence imaging experimental setup. An argon ion laser is shaped into a laser light sheet incident upon a microscope stage using a cylindrical lens and a microscope objective shown in Fig. 1b. Flood illumination is provided by a mercury arc lamp. Both the laser light and the arc-lamp light pass through electromechanical shutters with characteristic opening times of 1 ms and 10 ms, respectively. Electrokinetic flow is driven by a high-voltage power supply with current-monitoring feedback. Flow-field imaging is performed with a CCD camera. The shutters and data acquisition equipment are computer-controlled. **b** Detailed schematic of the optical setup. An epifluorescent microscope has been modified to include an additional dichroic mirror assembly, an electromechanical shutter (temporal resolution of 10 ms), and a cylindrical lens (f=5 cm). The upper dichroic mirror has bandpass color filters (excitation filter from 460 to 490 nm and barrier filter from 515 to 550 nm). The lower dichroic mirror has no color filters and is used to direct the photobleaching laser pulse. A circular argon ion laser beam (λ=488 nm) enters the back of the microscope and is directed into the flow field through a cylindrical lens and the objective. The laser is expanded by the cylindrical lens in one direction and then focused by the objective to form a laser sheet (Fig. 3)

(Olympus, Melville, N.Y.) that provides the stage for the capillary setup and contains the color filters, dichroic mirrors, and imaging optics. The light sources are an argon ion laser (output of 400 mW at 488 nm) and a broad-spectrum high-pressure mercury arc lamp. The laser provides a high-intensity light for photobleaching and the mercury lamp provides flood illumination. Both light sources are shuttered with electromechanical shutters (Vincent Associates, Rochester, N.Y.) with temporal resolutions of 2 ms and 10 ms for the laser and mercury lamp, respectively. The two CCD cameras used here were a back-illuminated CCD camera (PlutoCCD: 512×512-pixel resolution, 50-Hz frame rate, 12-bit depth; Pixelvision, Tigard, Ore.) and a 1,300×1,030-pixel Roper Scientific interline-transfer CCD camera (Trenton, N.J.). A high-voltage power supply (Kepco, Flushing, N.Y.) provides the electric fields needed for electrokinetic flow. Feedback on the current and voltage is provided by an especially built voltage and current monitoring circuitry combined with a DAQCard-1200 (National Instruments, Austin, Tex.) for data acquisition. All electronic devices are computer-controlled.

Figure 1b shows a detailed view of the optical setup. A fused-silica cylindrical lens with f=5 cm (Melles Griot, Irvine, Calif.) is adjacent to the lower dichroic mirror and expands the laser beam in a plane. The diverging laser sheet is then focused by a microscope objective (10× or 20× with NA=0.3 and 0.5, respectively) into a micro-light-sheet at the microchannel. Bandpass color filters in the upper dichroic mirror cube pass blue light from the mercury lamp to the microflow device and green light from the fluorescein to the camera. The mercury lamp is shuttered by an electromechanical shutter to reduce unwanted photobleaching during diffusion experiments.

Figure 2 shows the microflow device used for the combined electroosmotically and pressure-driven flow experiments. The device consists of a borosilicate capillary (Wilmad Glass, Buena, N.J.), plastic pipette tips (0.2 mL), electrode brackets, and a glass slide. The base of each electrode bracket has a 4-mm diameter hole (slightly smaller than the diameter of the pipette tip base). Each end of the capillary is pinned to the glass slide by an electrode bracket and an epoxy bond. Extra reservoir height can be achieved by adding plastic tubing. The capillaries have a square cross section of 50×50 μm and a length that varies from 4 to 14 cm. A second microflow device (not shown) is used for the electroosmotic flow experiments. The

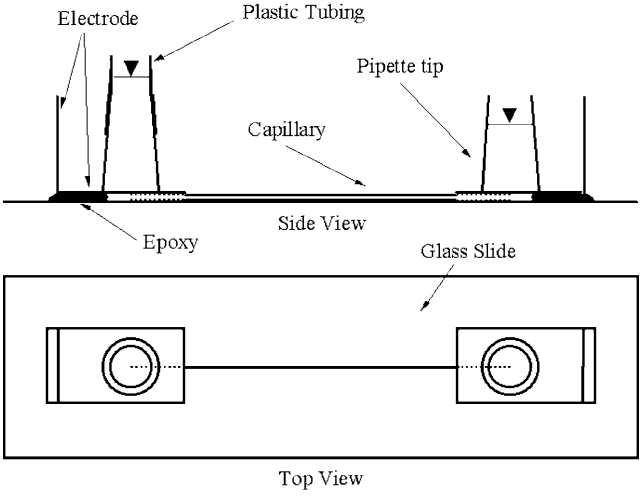

Fig. 2. Schematic of one of the microflow devices used in the current experiments. A glass capillary (50×50 μm cross section, 4–14 cm length) is epoxy-bonded at the ends to a glass slide. An electrode bracket (with a 4-mm-diameter hole in the base) is epoxy-bonded over each end of the capillary. The fluid reservoirs are plastic pipette tips epoxy-bonded on top of the electrodes. Additional reservoir height for the combined electroosmotically and pressure-driven flow is achieved by attaching plastic tubing to the pipette tip on the left

second device is similar to that shown in Fig. 2 except that the pipette tips are replaced with hollow glass cylinders (5 mm ID, 7 mm OD, and 7 mm long) and platinum wire electrodes (250 μm diameter) are inserted into the fluid reservoirs in place of the electrode brackets. The third microflow device investigated is an acrylic microfluidic chip described below.

Figure 3 shows a detailed schematic of the micro-light-sheet crossing a microchannel. A portion of the laser sheet perimeter, corresponding to the electric field contour at e^{-1} of the maximum, is shown. The x-y plane is parallel to the plane of the microscope stage and the bottom of the capillary. The theoretical widths at the beam waists in the x- and y-directions, b_x and b_y, respectively, are 8.8 μm and 490 μm for the 10× objective (4.4 μm and 250 μm for the 20× objective). These were calculated using the ABCD method (Siegman 1986) for Gaussian beam propagation. The corresponding theoretical collimated Rayleigh range for the beam waist, d_z, is 250 μm for the 10× objective and 63 μm for the 20× objective. Not shown in the figure is the collimated range for the other beam waist, which is 78 cm and 19 cm for the 10× and 20× objectives, respectively.

Borate buffer was created by mixing boric acid (Fischer Scientific, Pittsburgh, Pa.) with sodium hydroxide (Mallinckrodt, Phillipsburg, N.J) until pH 9 was achieved. Fluorescein sodium salt was purchased from Baker (Phillipsburg, N.J.) and 70 kDa and 2 MDa fluorescein-dextran conjugate was purchased from Molecular Probes (Eugene, Ore.). Fluorescein dye concentrations ranged from 0.1 to 1 mM. The fluorescence filter cube (Olympus, Melville, N.Y.) has an excitation bandpass filter from 460 to 490 nm and a barrier bandpass filter from 515 to 550 nm.

3
Experimental results

3.1
Diffusion of unphotobleached fluorophores

Several techniques can be used to estimate diffusion coefficients from dye images. First, the recovery of the peak intensity can be fit with the solution of the convection-diffusion equation (Jain et al. 1990). This technique was used extensively during the development of FRAP because photomultiplier tubes could easily track the recovery at the center of a bleach spot. As Salmon et al. (1984) report, this method has the disadvantage of being sensitive to the initial bleach profile and the duration of photobleaching relative to the fluorophore diffusive time scale. Second, numerical analysis may be used to directly calculate the derivatives in the convective-diffusion equation (Salmon et al. 1984). This method is not sensitive to the initial photobleach profile or duration of the photobleaching relative to the fluorophore diffusive time scale. Third, the statistical variance of the whole image can be calculated. This method has the advantage of not assuming a photobleached profile shape, but the disadvantage of being sensitive to background noise. Fourth, a Gaussian can be fit to a portion of the one-dimensional axial profile, and the time variation of the Gaussian standard deviation may be used to calculate the diffusion coefficient. The data fit should exclude the low-signal regions of the profile that are corrupted by background noise. The first, third, and fourth methods above were all applied to the current data and gave similar results. The fourth (Gaussian fit) method was chosen for data analysis because it is less sensitive to the effects of the unwanted photobleaching from the mercury lamp that may occur after the initial, high-intensity photobleaching event and has the same advantages as the second method described above.

Images were corrected by applying the following matrix operation to each fluorescence image: a darkfield background image was subtracted from each image and this difference was normalized by the difference between flatfield and darkfield images (Photometrics 1992).

$$I_{\text{corr}} = \frac{I_{\text{raw}} - I_{\text{df}}}{I_{\text{ff}} - I_{\text{df}}} \tag{7}$$

The corrected fluorescence intensity is assumed to be proportional to the fluorophore concentration. This assumption is reasonable provided that the fluorophore concentration is sufficiently dilute to avoid the inner filter and reabsorption effects (Tanke et al. 1982) and provided that the pH remains constant (Sjoback et al. 1995). For the stopped flow diffusion experiments, photobleaching due to the mercury lamp was minimized by shuttering between camera exposures. Using this technique, a diffusion coefficient of 9×10^{-8} $\text{cm}^2\times\text{s}^{-1}$ was obtained for 2 MDa fluorescein-dextran conjugate. This compares well with

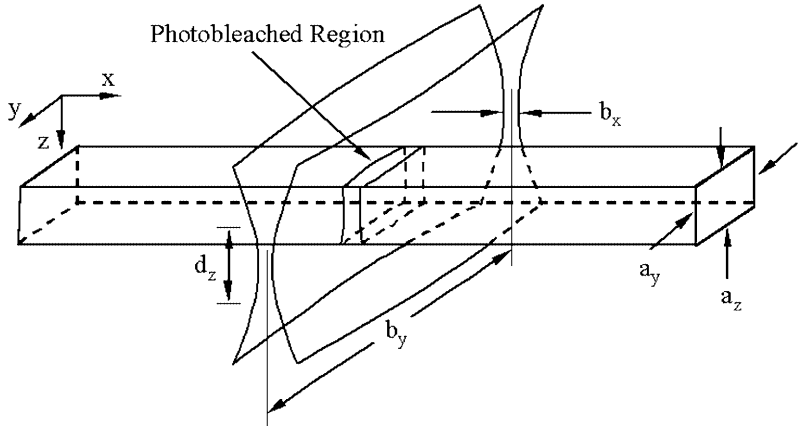

Fig. 3. Schematic of the micro-laser-sheet crossing the capillary and the resulting photobleached region (not to scale). The capillary has width a_y and depth a_z. The width of the beam waists in the x- and y-directions are b_x and b_y, respectively. The collimated range of the laser sheet is d_z. The photobleached region has a Gaussian intensity profile along the capillary axis and slight curvature in the y- and z-directions

7×10^{-8} $cm^2\times s^{-1}$ based on a power-law extrapolation of the diffusivity vs. molecular weight measurements for dextran molecules reported by Furukawa et al. (1991). The slightly larger measured diffusivity is expected because the dextran-fluorescein was vortexed (to aid dissolution) and then filtered with a 0.45-μm polypropylene filter (Cole-Parmer, Vernon Hills, Ill.); this procedure may have decreased the average chain length. The diffusion coefficient of fluorescein was measured to be 5×10^{-6} $cm^2\times s^{-1}$, which compares well with values reported by Paul et al. (1998), Moore and Jorgenson (1993), and Furukawa et al. (1991). Table 1 summarizes the diffusivities and mobilities of the various dyes we investigated and shows some comparisons with published data. The 20–50% uncertainties in the mean values reported in the table can be improved by ensemble averaging additional measurements.

3.2
Electroosmotic flow experiments

Figure 4 shows a photobleached line in a 50×50-μm cross section capillary (wall thickness=25 μm) immediately after photobleaching (Fig. 4a) and 0.53 s later (Fig. 4b). The image was acquired at 20× magnification and has been flatfield-corrected. The fluid was a 20-mM borate buffer (pH 9) with a 1-mM concentration of fluorescein. The camera exposure time was 16.4 ms and the photobleaching pulse duration was 10 ms. The electric field was 80 $V\times cm^{-1}$. Pressure-driven flow was minimized by balancing the heights of reservoir fluid. The figure shows how diffusion rapidly decreased the image SNR as the band progressed downstream. Gaussian curves were fit to the axial intensity profiles obtained from the experiment shown in Fig. 4. The intensity values on the ordinate of these plots is of the form $(I_o–I)$ where I is the intensity of the imaged, unphotobleached fluorophores, so that the Gaussian profiles have a maximum at the center of the photobleached band. Figure 5 shows a time sequence of column-averaged axial intensity profiles for the EOF experiment together with the appropriate Gaussian curve fits. Column-averaged profile refers to integrating the intensity values in the y-direction (e.g., Fig. 4) and then plotting a row dependence. The time between the curves is 75 ms (every 4th frame), and the first and last profiles correspond to the images in Fig. 4. Diffusion of fluorescein quickly reduced the image contrast, but column-averaged axial profiles have SNR>50 after 0.53 s, as seen in the right-most curve of Fig. 5. Note the typical $t^{-0.5}$ dependence of the curve maxima as the species diffuses. The EOF velocity was determined using the current monitoring technique described in the following section. The resulting Peclet number (ratio of convection to molecular diffusion with the channel width as the characteristic length) is Pe=40.

3.3
Fluorophore electrophoretic mobilities

The electrophoretic mobilities of several dyes were measured in a pH-9 borate buffer using a combination of the current monitoring method (Huang et al. 1988) and photobleached-fluorescence imaging. The velocity of a photobleached line, U_{APP}, (with respect to the lab frame) is the sum of the electrophoretic and electroosmotic velocities, U_{EP} and U_{EOF}, respectively. In the current monitoring method experiments, we measured the changing conductance of a microchannel as a buffer solution was displaced by a second buffer solution of 5% lower conductivity. The result of the displacement process is a linearly decreasing current, and the axially averaged electroosmotic mobility of the channel can be calculated from the rate of change of the current. A second calibration experiment was performed with a dye and buffer solution in order to study the effect of the dye on the electroosmotic mobility of the capillary. The difference in mobility in such cases was found to be negligible. Once the channel was calibrated in this manner, the electrophoretic mobility of the dye was determined from the difference of the velocity of the photobleached line, U_{APP}, and the electroosmotic velocity,

Table 1. Mobility and diffusivity data from the current experiments and comparisons with published data

Species	Mobility $[cm^2\times V^{-1}\times s^{-1}]$	Published Paul et al. (1998), Harrison et al. (1992)	Diffusivity $[cm^2\times s^{-1}]$	Published Paul et al. (1998), Moore and Jorgenson (1993), Furukawa et al. (1991)
Fluorescein	$-3\times10^{-4}\pm1$	-3.3×10^{-4}	$5\times10^{-6}\pm2$	4.4×10^{-6}, 6.4×10^{-6}
2-MDa Fluorescein-Dextran	-2×10^{-4} [a] ±1	–	$9\times10^{-8}\pm2$	7×10^{-8}
70-kDa Fluorescein-Dextran	$-3\times10^{-4}\pm1$, -5×10^{-4} [a] ±2	–	–	–

[a] lysine-fixable

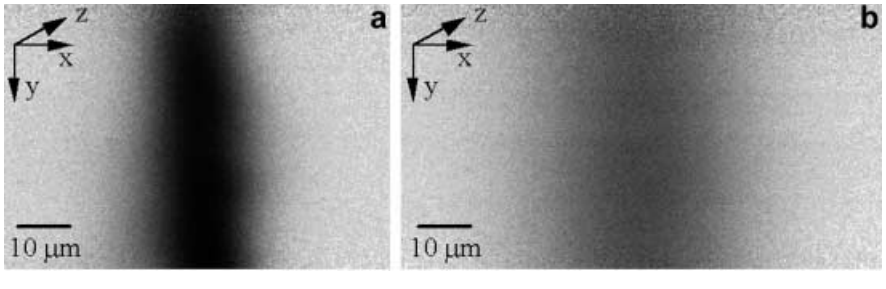

Fig. 4a, b. Flatfield-corrected images of a photobleached line in steady electroosmotic flow from left to right at time **a** t=0 s and **b** t=0.53 s. The electrolyte is a dilute solution of fluorescein in 20 mM borate buffer. The frame rate was 53 frames per second. The camera exposure time is 16.4 ms and the electric field is 80 $V\times cm^{-1}$. The images were acquired with a 20× objective (NA=0.5) and have been centered about the band

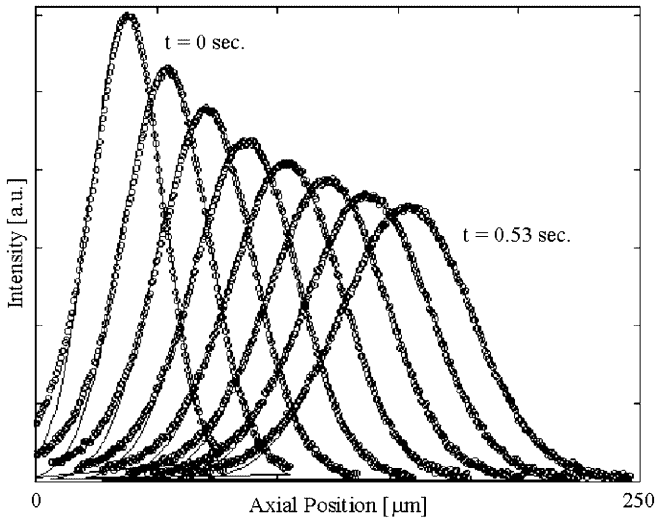

Fig. 5. Time sequence of column-averaged (in the *y*-direction on the CCD) axial intensity profiles for the EOF experiment shown in Fig. 4. The profiles are of the form (I_o–I), where I is the intensity of the imaged, unphotobleached fluorophores and I_o is a normalization constant, so that the profiles have a maximum at the center of the photobleached band. The data (*circles*) clearly show the Gaussian intensity distribution and the characteristic $t^{-0.5}$ diffusive decay of the curve maxima. Also shown are Gaussian fits to the data (*thin solid lines*), which are used to calculate the scalar diffusion coefficient and velocity. The time between each data set is 75 ms

U_{EOF}. The measured electrophoretic mobility of the 2-MDa lysine-fixable dextran-fluorescein conjugate was -2×10^{-4} $cm^2\times V^{-1}\times s^{-1}$ (positive mobility is defined as motion towards the cathode). We also determined the mobility of 70-kDa dextran-fluorescein conjugate, 70-kDa lysine-fixable dextran-fluorescein conjugate, and fluorescein. These measurements are listed in Table 1 along with comparisons of selected values from the literature. The electroosmotic mobility of the Pyrex (borosilicate) capillaries used in these measurements was measured as 5×10^{-4} $cm^2\times V^{-1}\times s^{-1}$ with a pH-9, 20-mM borate buffer. Thus, the apparent photobleached line motion of the fluorophores in Table 1 has a lower velocity than the electroosmotic bulk flow velocity. Harrison et al. (1992) and Paul et. al. (1998) reported electroosmotic mobilities of 5.07×10^{-4} $cm^2\times V^{-1}\times s^{-1}$ and 5.87×10^{-4} $cm^2\times V^{-1}\times s^{-1}$, respectively, for their fused-silica capillaries. The current values of electroosmotic and electrophoretic mobilities are in good agreement, as shown in Table 1.

An additional verification of the mobility can be made by applying the Nernst-Einstein equation (Probstein 1994)

$$D = \frac{RTv}{zN_Ae} \tag{8}$$

to relate the diffusivity, D, of fluorescein to its ionic mobility, v. Using a weighted average for the valence number (assuming 95% dianionic and 5% anionic at pH 9) (Sjoback et al. 1995) and assuming a diffusion coefficient of 5×10^{-6} $cm^2\times s^{-1}$ and a temperature of 300 K, this estimate gives $v_{ep}=-3.8\times10^{-4}$ $cm^2\times V^{-1}\times s^{-1}$. Table 1 summarizes the measured electrokinetic mobility data.

3.4
Combined electroosmotically and pressure-driven flow

Images of a photobleached zone in a capillary with an electroosmotic flow (to the right) in the presence of an adverse pressure gradient is shown in Fig. 6. The channel is 50×50 μm in cross section and 5 cm long. A height difference in liquid levels of 2 mm was applied (higher pressure on the right). An 80-$V\times cm^{-1}$ electric field was applied between the two end reservoirs. The observations presented here were made at a location 3 cm from the high-pressure reservoir where the flow is fully developed. The Reynolds number based on hydraulic diameter and maximum velocity in the channel was Re=0.3. The fluid was a 20-mM borate buffer with a dilute concentration (<1 mM) of 2-MDa fluorescein-dextran conjugate. The bleach pulse was 10 ms and the exposure time was 12 ms. The photobleached volume was exposed to a 0.12-mJ laser pulse which resulted in a 30% decrease in fluorescence intensity. Images were acquired with the 20× objective described above. The stretching and shearing of the fluid due to both in-plane and out-of-plane velocity gradients resulted in rapid dispersion of the fluorophores in the photobleached region.

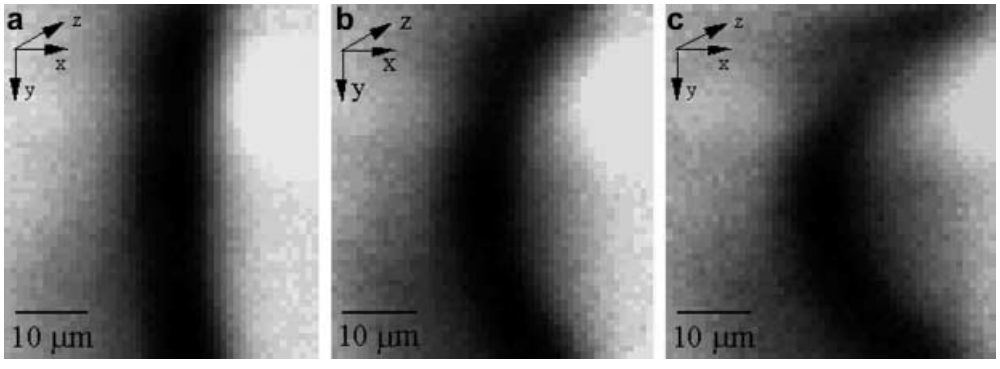

Fig. 6a–c. Combined electroosmotically and pressure-driven flow at time **a** t=0 s, **b** t=0.06 s, and **c** t=0.12 s. Electric potential and pressure decrease and increase, respectively, towards the right. The electric field is 80 $V\times cm^{-1}$, and the electrolyte is a dilute solution (<1 mM) of 2-MDa fluorescein-dextran conjugate in 20-mM borate buffer at pH 9. The capillary has a 50×50-μm cross section. Images were acquired with a 20× objective (NA=0.5) and 2×2-pixel binning. The images, acquired in the capillary frame of reference, show the band translating slowly to the right. The SNR decreases primarily because of advective dispersion of the band due to pressure-driven shear flow

3.5
Electrokinetic flow in a curved microchannel

As an example application of photobleached-fluorescence imaging in microfluidic systems, Fig. 7 shows a visualization of electrokinetic flow in a curved microchannel. The microchannel was fabricated in acrylic by ACLARA BioSciences, Inc. (Mountain View, Calif.) using a hot embossing method. The channel was trapezoidal in cross section, with a top width of 110 microns, a bottom width of 32 microns, and a depth of 50 microns. The images were acquired with a 10× objective (*NA*=0.3) using the interline-transfer CCD camera. The electric field along the centerline was 30 V×cm^{-1}. The dye was a 2-MDa dextran-fluorescein conjugate in a 20-mM borate buffer. The image sequence shows the photobleached line stretching and tilting as it develops downstream. This dispersion occurs because the inner radius had a higher electric field and a shorter path length, resulting in the so-called 'racetrack' effect (Culbertson et al. 1998; Griffiths and Nilson 2000; Griffiths and Nilson 2001; Molho et al. 2001; Paegel et al. 2000). Figure 8 shows a simulation of electroosmotic flow in a curved two-dimensional microchannel performed with CFDRC (CFD-GUI version 6.2.3, CFD Research Corporation, Huntsville, Ala.), a commercial software simulation package. For a uniform concentration field as in the current investigation, the solution methodology employed by this code is equivalent to applying a wall slip boundary condition with velocity determined by the Helmholtz-Smoluchowski equation:

$$u = -\frac{\varepsilon\zeta E}{\mu}, \tag{9}$$

where u is the electroosmotic velocity, ϵ is the permittivity, ζ is the zeta potential, E is the electric field, and μ is the dynamic viscosity. Boundary conditions applied in the simulation include a uniform inlet potential (5 V) and a uniform outlet potential (0 V). The side walls were specified to be electrically insulating with a zeta potential of ζ=–80 mV. This value is an estimate based on the velocity of the photobleached line over the course of the turn and our measurements of the electrophoretic mobility of dextran-fluorescein conjugate. The pressures at the inlets and outlets of the solution domain were uniform. In the simulation, the scalar diffusion coefficient of the tracer was specified as negligibly small in order to simulate the high-Peclet-number dispersion associated with experimental conditions (*Pe*=14,000 based on a length scale of 100 microns and diffusivity of 7×10^{-8} cm^2×s^{-1}). There was significant numerical diffusion as a result of the finite grid spacing (average pixel length scale of 4 μm), so that the simulation had an effective diffusion coefficient roughly 100 times larger than the experiment. However, in both cases, the Peclet number is sufficiently large for band dispersion to be dominated by advection and relatively insensitive to diffusion (Molho et al. 2001). Figure 8 demonstrates that the simulation qualitatively predicts the band distortion seen in Fig. 7.

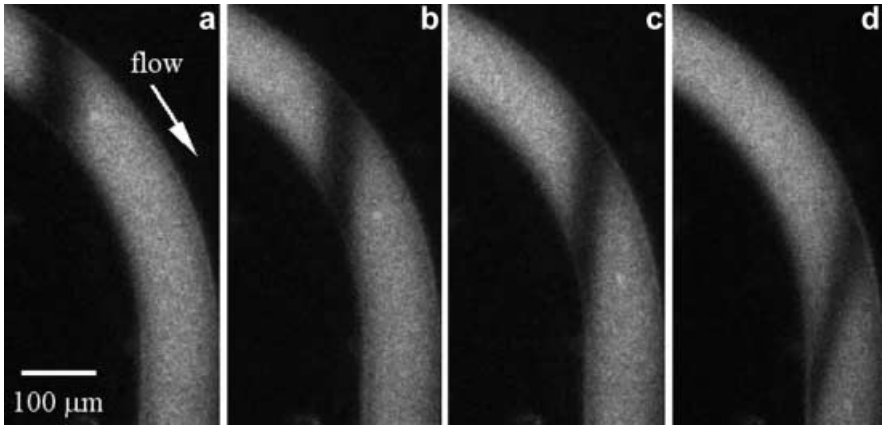

Fig. 7a–d. Electroosmotic flow from top to bottom in a curved acrylic microchannel at time **a** *t*=0 s, **b** *t*=1.2 s, **c** *t*=1.8 s, and **d** *t*=3.2 s. The electric field is 30 V×cm^{-1}. The electrolyte is a 20-mM borate buffer with a dilute (<1 mM) 2-MDa dextran-fluorescein conjugate. The channel has a trapezoidal cross section with a depth of 50 microns and a bottom width of 32 microns. Images were acquired with a 10× objective (*NA*=0.3). The stretching and tilting of the photobleached region is due to the so-called 'racetrack' effect, which occurs because the inside radius has a higher electric field and shorter path length than the outside radius

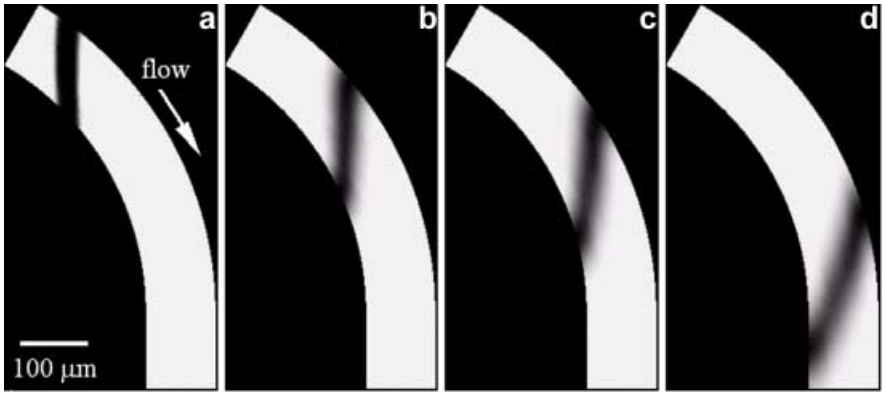

Fig. 8a–d. Simulation of electroosmotic flow in a two-dimensional curved microchannel. The boundary conditions at the inlet and outlet are uniform electric potential and pressure (5 V at the top and 0 V at the bottom). The walls are electrically insulating and have a zeta potential of –80 mV. Despite the effects of numerical diffusion, the overall band dispersion is dominated by advection (i.e., relatively independent of molecular diffusion) and similar to the actual dispersion shown in Fig. 7

4 Conclusions

Photobleached-fluorescence imaging is an in-situ, non-invasive technique for measuring planar microscale flows in transparent microdevices using visible-wavelength laser light. Quantitative diffusion and advection information can be obtained in electrokinetic and pressure-driven flows by performing a series of calibration experiments to quantify the transport characteristics of the dye. The photobleached line shape is controlled using a cylindrical lens together with microscope optics and a shuttering system. The spatial and temporal resolution of the technique are determined by photobleaching time (10 ms), the time between frames of the imaging system (19 ms), and the width of the laser sheet used to effect bleaching (less than 10 μm). The Peclet number associated with the flow visualization may be adjusted using dyes with a wide range of diffusive properties. Effective use of the photobleached-fluorescence visualization technique requires consideration of diffusion and shear-driven dispersion, the collimated range of the laser sheet relative to the microdevice length scale, fluorophore concentration (which must be dilute enough to avoid the inner filter effect and reabsorption effects), laser heating/destruction of sample streams, and disturbance of the flow through heat absorption. Advantages include the ability to track undisturbed fluorophores (in the dilute limit), investigate microfluidic systems transparent to visible laser light (e.g., polymer systems), and utilize fluorophores already present in many bioanalytical assays. The dye diffusivities and mobilities we have measured are in good agreement with published data. Application of the technique to electrokinetic flow in a curved microchannel shows the 'racetrack' effect that adds skew and dispersion to an analyte band. While out-of-plane velocity gradients can rapidly reduce the SNR of photobleached measurements, microchannel flows with largely two-dimensional velocity fields such as electrokinetic flow in curves or through intersections are good candidates for the technique.

References

Axelrod D (1977) Cell surface heating during fluorescence photobleaching recovery experiments. Biophys J 18:129–131

Axelrod D, Koppel DE, Schlessinger J, Elson EL, Webb WW (1976) Mobility measurement by analysis of fluorescence photobleaching recovery kinetics. Biophys J 16:1055–1069

Bello MS (1996) Electrolytic modification of a buffer during a capillary electrophoresis run. J Chromat A 744:81–91

Culbertson CT, Jacobson SC, Ramsey JM (1998) Dispersion sources for compact geometries on microchips. Anal Chem 70:3781–3789

Dolnik V, Liu SR, Jovanovich S (2000) Capillary electrophoresis on microchip. Electrophoresis 21:41–54

Effenhauser CS (1998) Integrated chip-based microcolumn separation systems. Top Curr Chem 194:51–82

Falco RE, Chu CC (1987) Measurement of two-dimensional fluid dynamic quantities using a photochromic grid-tracing technique. SPIE 814:706–710

Furukawa R, Arauz-Lara JL, Ware BR (1991) Self-diffusion and probe diffusion in dilute and semidilute aqueous solutions of dextran. Macromolecules 24:599–605

Griffiths SK, Nilson RH (2000) Band spreading in two-dimensional microchannel turns for electrokinetic species transport. Anal Chem 72:5473–5482

Griffiths SK, Nilson RH (2001) Low dispersion turns and junctions for microchannel systems. Anal Chem 73:272–278

Harrison DJ, Manz A, Fan ZH, Ludi H, Widmer HM (1992) Capillary electrophoresis and sample injection systems integrated on a planar glass chip. Anal Chem 64:1926–1932

Herr AE, Molho JI, Santiago JG, Mungal MG, Kenny TW, Garguilo MG (2000) Electroosmotic capillary flow with nonuniform zeta potential. Anal Chem 72:1053–1057

Huang X, Gordon MJ, Zare RN (1988) Current-monitoring method for measuring the electroosmotic flow rate in capillary zone electrophoresis. Anal Chem 60:1837–1838

Jain RK, Stock RJ, Chary SR, Rueter M (1990) Convection and diffusion measurements using fluorescence recovery after photobleaching and video image analysis: in vitro calibration and assessment. Microvasc Res 39:77–93

Koochesfahani MM, Cohn RK, Gendrich CP, Nocera DG (1996) Molecular tagging diagnostics for the study of kinematics and mixing in liquid phase flows. In: Adrian RJ, Durao DFG, Durst F, Heitor MV, Maeda M, Whitelaw JH (eds) International Symposium on Applications of Laser Techniques to Fluid Mechanics, 1996, Lisbon, Portugal. pp 125–144

Lanni F, Ware BR (1982) Modulation detection of fluorescence photobleaching recovery. Rev Sci Inst 53:905–908

Lempert WR, Magee K, Ronney P, Gee KR, Haughland RP (1995) Flow-tagging velocimetry in incompressible flow using photoactivated nonintrusive tracking of molecular motion (PHANTOMM). Exp Fluids 18:249–257

Manz A, Harrison DJ, Verpoorte E, Widmer HM (1993) Planar chips technology for miniaturization of separation systems: a developing perspective in chemical monitoring. Adv Chromatogr 33:1–66

Molho JI, Herr AE, Mosier BP, Santiago JG, Kenny TW, Brennen RA, Gordon GB, Mohammadi B (2001) Optimization of turn geometries for microchip electrophoresis. Anal Chem 73:1350–1360

Monnig CA, Jorgenson JW (1991) On-column sample gating for high-speed capillary zone electrophoresis. Anal Chem 63:802–807

Monnig CA, Dohmeier DM, Jorgenson JW (1991) Sample gating in open tubular and packed capillaries for high-speed liquid chromatography. Anal Chem 63:807–810

Moore AW, Jorgenson JW (1993) Study of zone broadening in optically gated high-speed capillary electrophoresis. Anal Chem 65:3550–3560

Paegel BM, Hutt LD, Simpson PC, Mathies RA (2000) Turn geometry for minimizing band broadening in microfabricated capillary electrophoresis channels. Anal Chem 72:3030–3037

Paul PH, Garguilo MG, Rakestraw DJ (1998) Imaging of pressure- and electrokinetically driven flows through open capillaries. Anal Chem 70:2459–2467

Periasamy N, Bicknese S, Verkman AS (1996) Reversible photobleaching of fluorescein conjugates in air-saturated viscous solutions: singlet and triplet state quenching by tryptophan. Photochem Photobiol 63:265–271

Photometrics Ltd. (1992) Charged-coupled devices for quantitative electronic imaging, Rev H. Photometrics Ltd, Tucson, Ariz.

Probstein RF (1994) Physicochemical Hydrodynamics: An Introduction. 2nd ed. Wiley, New York

Salmon ED, Saxton WM, Leslie RJ, Karow ML, McIntosh JR (1984) Diffusion coefficient of fluorescein-labeled tubulin in the cytoplasm of embryonic cells of a sea urchin. Video image analysis of fluorescence redistribution after photobleaching. J Cell Biol 99:2157–2164

Saylor JR (1995) Photobleaching of disodium fluorescein in water. Exp Fluids 18:445–447

Schrum KF, Lancaster JM, Johnston SE, Gilman SD (2000) Monitoring electroosmotic flow by periodic photobleaching of a dilute, neutral fluorophore. Anal Chem 72:4317–4321

Siegman AE (1986) Lasers. University Science Books, Mill Valley, Calif.

Simon JR, Gough A, Urbanik E, Wang F, Lanni F, Ware BR, Taylor DL (1988) Analysis of rhodamine and fluorescein labeled F-actin diffusion in vitro by fluorescence photobleaching recovery. Biophys J 54:801–815

Sjoback R, Nygren J, Kubista M (1995) Absorption and fluorescence properties of fluorescein. Spectrochim Acta A Biomol Spectrosc 51:L7–L21

Song L, Hennink EJ, Young IT, Tanke HJ (1995) Photobleaching kinetics of fluorescein in quantitative fluorescence microscopy. Biophys J 68:2588–2600

Tanke HJ, Oostveldt P van, Duijn P van (1982) A parameter for the distribution of fluorophores in cells derived from measurements of inner filter effect and reabsorption phenomenon. Cytometry 2:359–369
Tsay TT, Jacobson KA (1991) Spatial Fourier analysis of video photobleaching measurements: principles and optimization. Biophys J 60:360–368
Wang GR, Fiedler HE (2000a) On high-spatial-resolution scalar measurement with LIF. Part 1: Photobleaching and thermal blooming. Exp Fluids 29:257–264
Wang GR, Fiedler HE (2000b) On high-spatial-resolution scalar measurement with LIF. Part 2: The noise characteristic. Exp Fluids 29:265–274